International Journal of Fluid Machinery and Systems
Vol. 7, No. 4, October-December 2014

DOI: http://dx.doi.org/10.5293/IJFMS.2014.7.4.174
ISSN (Online): 1882-9554

Original Paper

The Flow Field of Undershot Cross-Flow Water Turbines Based on PIV Measurements and Numerical Analysis

Yasuyuki Nishi[1], Terumi Inagaki[2], Yanrong Li[2], Ryota Omiya[3] and Kentaro Hatano[3]

[1]Department of Mechanical Engineering, Ibaraki University
4-12-1 Nakanarusawa-cho, Hitachi-shi, Ibaraki, 316-8511, Japan, y-nishi@mx.ibaraki.ac.jp
[2]Department of Mechanical Engineering, Ibaraki University
4-12-1 Nakanarusawa-cho, Hitachi-shi, Ibaraki, 316-8511, Japan
[3]Graduate School of Science and Engineering, Ibaraki University
4-12-1 Nakanarusawa-cho, Hitachi-shi, Ibaraki, 316-8511, Japan

Abstract

The ultimate objective of this study is to develop a water turbine appropriate for low-head open channels to effectively utilize the unused hydropower energy of rivers and agricultural waterways. The application of a cross-flow runner to open channels as an undershot water turbine has been considered and, to this end, a significant simplification was attained by removing the turbine casing. However, the flow field of an undershot cross-flow water turbine possesses free surfaces, and, as a result, the water depth around the runner changes with variation in the rotational speed such that the flow field itself is significantly altered. Thus, clear understanding of the flow fields observed with free surfaces to improve the performance of this turbine is necessary. In this study, the performance of this turbine and the flow field were evaluated through experiments and numerical analysis. The particle image velocimetry technique was used for flow measurements. The experimental results reflecting the performance of this turbine and the flow field were consistent with numerical analysis. In addition, the flow fields at the inlet and outlet regions at the first and second stages of this water turbine were clarified.

Keywords: Water Turbine, Cross-Flow Turbine, Open Channel, Free Surface, Particle Image Velocimetry, Numerical Analysis

1. Introduction

The effective use of renewable energy has been intensely investigated in recent years, and small hydropower generation has attracted attention in addition to photovoltaics, wind power generation, geothermal power generation, etc. Water turbines used in hydroelectric power generation can be broadly classified as water turbines that employ enclosed conduits (penstocks) [1,2] to conduct water at high and low heads, and those for use in open channels [3-5] with low and ultra-low heads. Water turbines employing penstocks are widely used in hydroelectric power generation, especially in large-scale centralized power generation involving water storage reservoirs, balancing reservoirs, and pipelines. However, it is currently difficult to carry out new construction because of a decline in suitable construction locations and concerns regarding the effects on the surrounding ecosystem.

In contrast, water turbines for use in open channels are directly installed in locations such as agricultural water channels and small-scale rivers, and these turbines require almost no auxiliary equipment. This approach minimizes the burden on the environment while facilitating easy serviceability. However, these turbines are characterized by low turbine efficiency and excessive outer diameters relative to the water depth, and have thus been mainly used as a source of motive force until now. In addition, the flow fields of water turbines for use in open channels possess free surfaces, and, as a result, the water depth around the runner changes with variation in the rotational speed such that the flow field itself is significantly altered. Present design methods are far from established. Therefore, it is necessary to clarify the complicated flow fields involving free surfaces in order to design water turbines of high efficiency and high rotational speed for use in open channels. With the development of computational fluid dynamics technology, the flow fields involved with various water turbine designs, such as a cross-flow water turbine [6,7] for use with penstocks and a spiral water turbine [8,9] for use in open channels, have been investigated by numerical analysis. However, the treatment of a flow field involving a free surface must efficiently and correctly capture the interface between the fluids of water and air. In addition, the flow fields involving a rotating runner are very complicated and numerical analyses remain problematic. Therefore, few such studies of these complex analyses have

Received June 12 2014; revised September 18 2014; accepted for publication October 5 2014: Review conducted by Prof. Le-Qin Wang. (Paper number O14018C)
Corresponding author: Yasuyuki Nishi, Professor, y-nishi@mx.ibaraki.ac.jp

been reported.

Under such a background, we focused our attention on runners in cross-flow turbines [10,11] used with penstocks under intermediate and low head conditions with the aim of developing a water turbine for use in open channels, which is also suitable for ultra-low heads. Substantial simplification was attained in the analysis by eliminating the guide vane, casing, etc., and a cross-flow turbine was applied to an open channel as an undershot water turbine [12,13]. The performance of the cross-flow turbine (undershot cross-flow turbine) installed in an open channel was experimentally clarified [12,13].

In this study, a combination of particle image velocimetry (PIV) measurements and numerical analysis is used to investigate the flow fields involving the free surface of an undershot cross-flow water turbine.

2. Experimental Apparatus and Method

The test runner [12,13] used in this study is illustrated in Fig. 1, and its specifications are presented in Table 1. The runner has the following dimensions: outer diameter D_1 = 0.18 m, width b = 0.24 m, clearance between runner and side walls γ = 5 mm, and clearance between runner and floor δ = 5 mm. Other specifications for this runner were determined in reference to a typical cross-flow runner [11] used in conjunction with a penstock. The circumferential angle θ defined the negative direction of the X-axis as θ = 0° and the counterclockwise rotation as positive. On the outer circumference of the runner, the measuring points of the flow were prepared at a position shifted 9 mm toward the path direction on the outer side. Moreover, on the inner circumference of the runner, the measuring points of the flow were prepared at a position shifted 9 mm towards the path direction on the inner side.

A summarized illustration of the experimental apparatus is shown in Fig. 2. The equipment used in this experiment consisted of an open-air circulation water tank that was used to simulate an open channel. The experiment was conducted under a condition setting with the flow rate set to Q = 0.003 m^3/s. The flow rate Q was measured using an electromagnetic flow meter. The load on the water turbine was altered using a load machine, and the rotational speed n and torque T were measured using an electromagnetic pickup and a torque meter, respectively, from which we obtained the output power P. Water depth was measured at 2 points, upstream and downstream from the runner, providing for an upstream water depth h_3 and a downstream water depth h_4. These depths were derived through measurements obtained at a distance of $2D_1$ from the center of the runner in both the upstream and downstream directions. Measurements at each location were obtained from a point on the wall surface and from the center point of the channel having a width B = 0.25 m. In addition, both the upstream and downstream flow velocities, v_3 and v_4, respectively, were obtained using the measured upstream water depth h_3, the measured downstream water depth h_4, and the flow rate Q via the following equations.

$$v_3 = Q/(Bh_3) \tag{1}$$

$$v_4 = Q/(Bh_4) \tag{2}$$

In this study, the test runner and side walls of the open channel were made from transparent acrylic. A green diode-pumped solid-state high-power laser (CVI Melles Griot, 85-GHS-309, 3 W, 532 nm) was used as a light source to visualize the flow field around the test runner. Nylon 12 with a diameter of around 100 μm and a specific gravity of 1.02 was used as tracer particles. The runner width central was illuminated by the laser sheet. Original images were acquired at a spatial resolution of 800 × 600 pixels. The region around the test runner was divided into three parts and time series images were recorded at a recording speed of 200 or 500 fps depending on the local velocity by a high speed camera (Katokoken Co. Ltd., k-III). Based on the recorded images, the flow field around the test runner was post-processed using the direct cross-correlation method provided in the Flow Expert software package (Katokoken Co. Ltd., ver. 1.1.2.0).

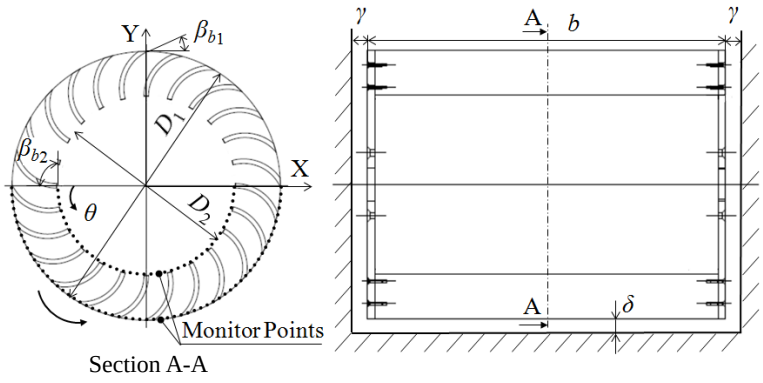

Fig. 1 The test runner

Table 1 Specifications of the test runner

Outer diameter: D_1	0.18 m
Inner diameter: D_2	0.12 m
Inlet angle: β_{b1}	30°
Outlet angle: β_{b2}	90°
Runner width: b	0.24 m
Side clearance: γ	5 mm
Bottom clearance: δ	5 mm
Number of blades: Z	24

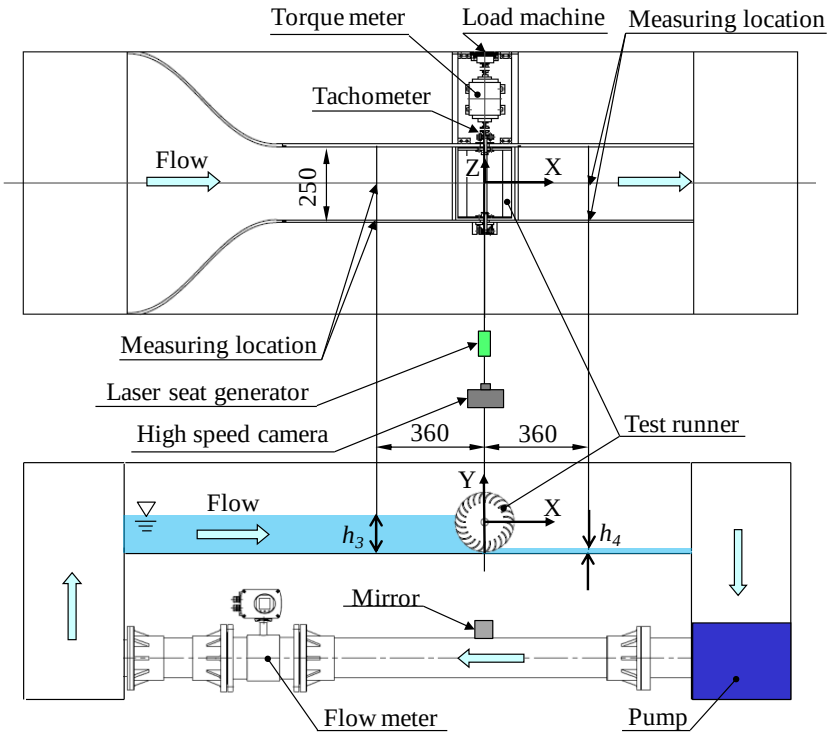

Fig. 2 Experimental apparatus

3. Method and Conditions for the Numerical Analysis

In this study, a three-dimensional unsteady flow analysis was conducted using the ANSYS CFX 13.0 general-purpose analysis code. The working fluids were water and air. In order to simulate the flow field involving a free surface, the uniform model [14] of an Euler–Euler simulation was applied as a multiphase flow model. The basic equations used in the model are based upon mass, momentum, and volume conservation [14]. The standard k–ε model was adopted as the turbulent flow model, and the standard wall function was used to handle regions near wall surfaces.

The computational domain of the simulated system and the computational grid of the test runner are shown in Figs. 3 and 4, respectively. The computational domain is composed of the runner and the upstream and downstream domains. The length of the upstream and downstream domains to the center of the runner is $9D_1$ and $10D_1$, respectively. Control surfaces are established at a distance of $2D_1$ in the upstream and downstream directions from the runner center. The velocity and depth of the water are monitored at these control surfaces as they would be in an experiment. The computational grid includes 462,000 elements in the runner domain, and about 420,000 combined elements in the upstream and downstream domains. Therefore, the computational grid includes a total of about 882,000 elements. For boundary conditions, the mass flow rate was applied to the inlet boundary, free outflow (with a relative air pressure of 0 Pa) was applied to the outlet boundary, and rotational speed was applied to the runner domain. In addition, the top surface of the computational domain was permeable to the atmosphere in order to allow air to move freely in and out of the computational domain, while non-slip conditions were applied to all the other walls. The boundary of the rotational and static domains was joined by the transient rotor–stator method [15]. For initial conditions, the experimental value of the upstream flow velocity v_3 was used as the flow velocity in the simulations. The volume fraction VF_{ih} of water was defined in accordance with the following formula using the step function.

$$VF_{ih} = step(h - y) \tag{3}$$

Here, y is the coordinate of the height direction in the computational domain, and the water depth h uses the experimental value of the upstream water depth h_3 in the simulations. Therefore, the position $y \leq h_3$ is the domain of water and the position $y > h_3$ is the domain of air. In addition, the time step was adjusted to ensure that the runner would undergo one rotation every 180 steps, and the time step was recalibrated until fluctuations in the flow became negligible.

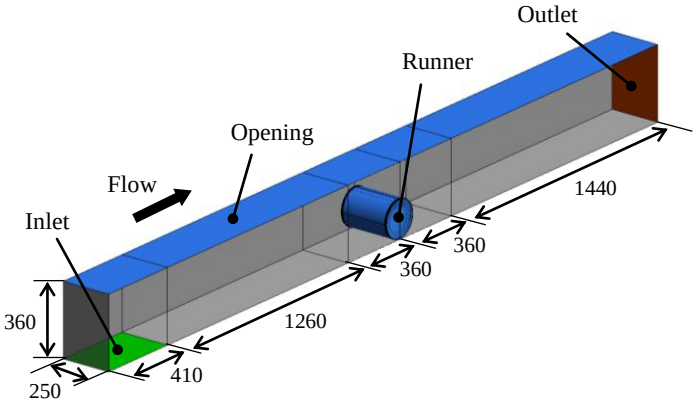

Fig. 3 Computational domain

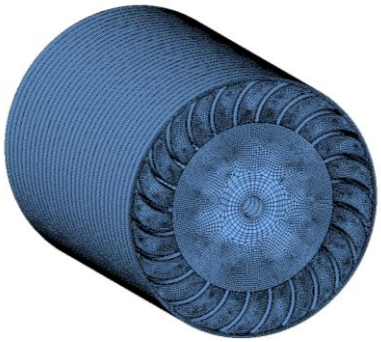

Fig. 4 Computational grid of the runner

4. Experimental and Analytical Results and Discussion

4.1 Comparison of Water Turbine Performance

Comparisons of the experimental and calculated values of water turbine performance are shown in Fig. 5. Both the experimental and calculated values of the torque T decrease with increasing rotational speed n. However, the calculated value of T exhibits a higher value than the experimental value over the entire range of rotational speeds. Hence, the calculated value of the output power P is also higher than the experimental value for all rotational speeds. In order to investigate this difference, the torque was measured when there was no runner, and the value obtained was nearly in agreement with the torque difference between the calculated and experimental values. Therefore, although it has an influence on a multiphase, turbulent flow model, the torque reduction by mechanical friction loss in the experiment is not considered in the simulation. This would seem to account for the observed differences between the calculated and experimental values for T.

Comparisons of the time averaged values of the upstream water depth h_3 and the downstream water depth h_4 determined by experiment and numerical analysis are shown in Fig. 6. Additionally, comparisons of the time averaged values of the upstream Froude number Fr_3 and the downstream Froude number Fr_4 determined by experiment and numerical analysis are shown in Fig. 7. The Froude number is a dimensionless value indicative of the resistance of a partly submerged object passing through water. Here, the upstream Froude number Fr_3 and the downstream Froude number Fr_4 are obtained using the following equations, respectively.

$$Fr_3 = v_3 \Big/ \sqrt{g h_3} \tag{4}$$

$$Fr_4 = v_4 \Big/ \sqrt{g h_4} \tag{5}$$

From Fig. 6, both the experimental and calculated values of the upstream water depth h_3 decrease with increasing rotational speed, and the downstream water depth h_4 correspondingly increases. This is considered to be due to the fact that the resistance of the runner to water flow decreases with increasing rotational speed. However, the downstream water depth h_4 is observed to increase rapidly in the neighborhood of n = 22–25 min^{-1}, and even if the rotational speed further increases, h_4 exhibits a fairly steady value. In this region of rotational speed, as shown in Fig. 7, the downstream Froude number is fairly constant as well at $Fr_4 < 1$. This indicates that the flow transitioned at this point from a supercritical flow to a subcritical flow. Although the rotational speeds observed by experiment and numerical analysis over this region of transition from supercritical to subcritical flow are different, the water depth and Froude number of the experimental and calculated values are satisfactorily in agreement. In addition, $Fr_3 < 1$ over the full range of rotational speed, and the upstream flow shows little dependency on the rotational speed, indicative of subcritical flow.

As mentioned previously, the water turbine performance is considered to have been captured to some extent in the numerical analysis.

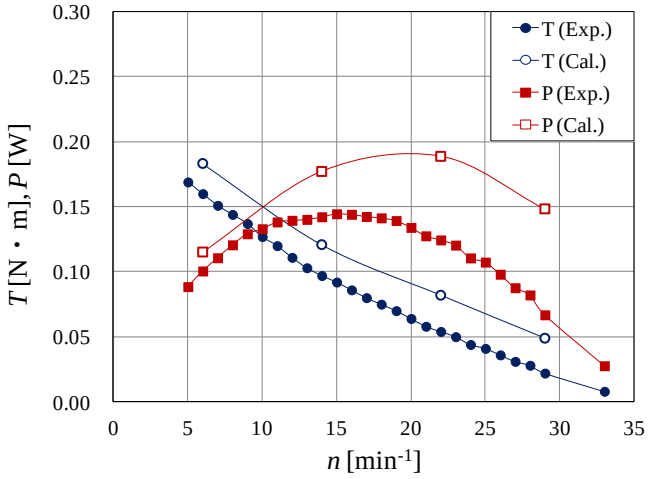

Fig. 5 Torque and power performance curves as a function of rotational speed from experiment and numerical analysis

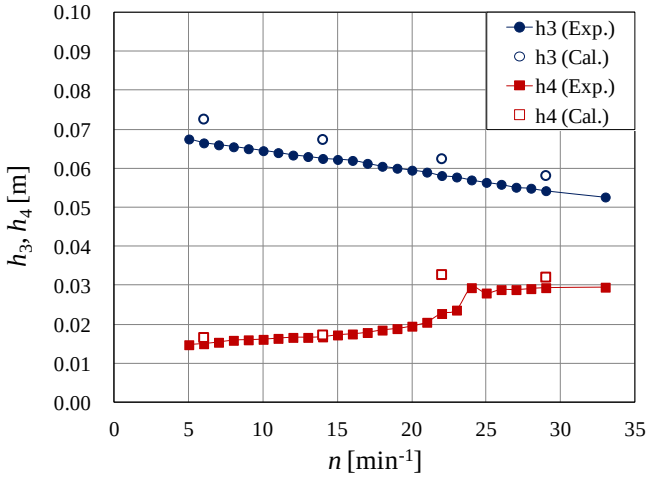

Fig. 6 Correlation between the rotational speed and both the upstream (h_3) and downstream (h_4) water depths from experiment and numerical analysis

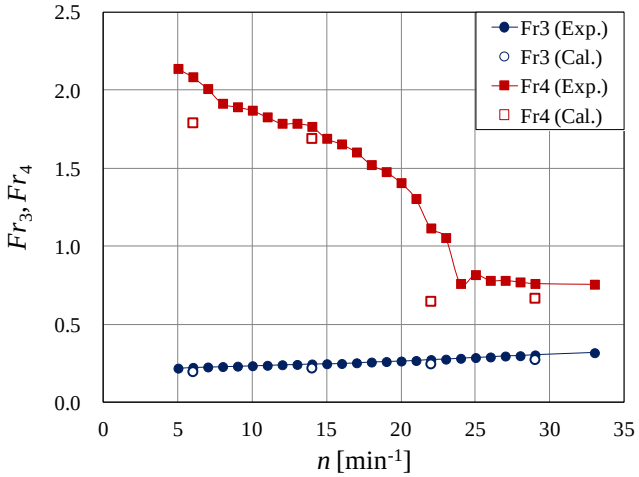

Fig. 7 Correlation between the rotational speed and both the upstream (Fr_3) and downstream (Fr_4) Froude numbers from experiment and numerical analysis

4.2 Comparison of the Flow Fields

The undershot cross-flow water turbine used by this study differs from cross-flow water turbines [6,7,10,11] for use with penstocks. Since there is no casing covering the runner, the interface between the water and air changes, particularly at the inlet and outlet regions of the runner. In general, since the flow field of a cross-flow runner is two dimensional, it is examined by considering the flow field in the runner width central at a rotational speed of n = 22 min^{-1}.

The absolute velocity vectors at the circumference of the runner, as determined by experiment and numerical analysis, are shown in Figs. 8 (a) and (b), respectively. However, the region near the bottom of the channel cannot be experimentally visualized on account of the experimental apparatus. The experimental and calculation results of the flow fields containing water depth are qualitatively in agreement. At the low θ region of the first stage outlet, the phenomenon in which water flows backwards between the back blades is captured by the calculations in a similar manner as observed experimentally. Furthermore, in the second stage outlet region, it is clear that the direction of flow has rapidly converted to the mainstream direction.

In order to determine the water and air interface, the time averaged values of the volume fractions, VF_1 and VF_2, of the water at the runner's outer and inner circumferences, respectively, as determined by numerical analysis, are shown in Fig. 9. Here, VF = 1 is water, VF = 0 is air, and VF = 0.5 is an interface of water and air. From Fig. 9, the regions of water at the outer and inner circumferences of the runner are determined as θ = 21°–129° and θ = 45°–132°, respectively.

The velocity triangles of the undershot cross-flow water turbine are shown in Fig. 10. Here, v_r defines the inside of the radial direction as positive. Moreover, the absolute flow angle α and the relative flow angle β define the rotational direction (counterclockwise rotation) of the runner as positive.

The time averaged values of the radial component v_{r1} and the circumferential component v_{u1} of the absolute velocity at the outer circumference of the runner are shown in Figs. 11 (a) and (b), respectively, as determined by both experiment and numerical analysis. On account of the experimental apparatus, as discussed previously, the experimental values of v_{r1} and v_{u1} are obtained only for the region of water evaluated by the time series images (i.e., only points lying outside $75° < \theta < 105°$). Moreover, the calculated values of v_{r1} and v_{u1} are exhibited only for the region of water determined from the abovementioned volume fraction. From Fig. 11 (a), the calculated value of v_{r1} gradually decreases with increasing θ, eventually reaching negative values. At the outer circumference of the runner, v_{r1} is positive in the first stage inlet region, and it is negative in the second stage outlet region. In the first stage inlet region within the measured limits, the experimental and calculated values of v_{r1} are mostly in agreement. At the second stage outlet region, although the tendency for the calculated values of v_{r1} to decrease with increasing θ is in agreement with the experimental values, the calculated values of v_{r1} are slightly larger than the experimental values.

From Fig. 11 (b), the calculated value of v_{u1} increases with increasing θ, and, after obtaining a maximum, it decreases slightly. At the first stage inlet region, the experimental and calculated values of v_{u1} are mostly in agreement. It is understood that the relative flow angle is not uniform because v_{r1} decreases, while v_{u1} increases with increasing θ in this region. Therefore, it is assumed that the shock losses at the first stage inlet increase. At the second stage outlet region, although the tendency for the calculated values of v_{u1} to decrease with increasing θ is in agreement with the experimental values, the calculated values are slightly smaller than the experimental values. The second stage outlet region is where the reversal flow containing the leakage flow of the bottom and the cross-flow intersect. In addition, the water depth is shallow and the depth undergoes substantial periodical fluctuations. Thus, because the phenomenon represents a complicated and unsteady flow field, it is not thought to have been fully captured by the calculations. In addition, since v_{u1} is very large in the low θ region of the second stage outlet, increase in waste losses is implied. To reduce these losses, the inlet angle β_{b1} needs to be optimized. However, since such change will also have an impact on the shock losses at the first stage inlet, these issues must be considered during the optimization process.

The time averaged values of the radial component v_{r2} and the circumferential component v_{u2} of the absolute velocities at the inner circumference of the runner are shown in Figs. 12 (a) and (b), respectively, as determined by both experimental and numerical analysis. The experimental and calculated values of v_{r2} increase with increasing θ, and, after obtaining a maximum, they decrease and become negative. At the inner circumference of the runner, v_{r2} is positive in the first stage outlet region and is negative in the second stage inlet region. At the first stage outlet and second stage inlet regions, within the limits that were measured, the experimental and calculated values of v_{r2} and v_{u2} are mostly in agreement. The calculated value of v_{u1} is negative in the low θ region of the first stage outlet. This trend appears to be due to a phenomenon we described earlier, in which water flows backwards between the back blades. Accordingly, outlet angle β_{b2} must be determined in a manner that considers this backflow and the shock losses at the second inlet.

As mentioned previously, it is clear that the PIV measurement results and calculated results of the flow fields of this water turbine are satisfactorily in agreement. Moreover, the flow fields at the inlet and outlet regions at the first and second stages of this water turbine were clarified. It is thought that the presented experimental and numerical results can greatly contribute to the elucidation of the complicated flow fields involving the free surfaces of this water turbine.

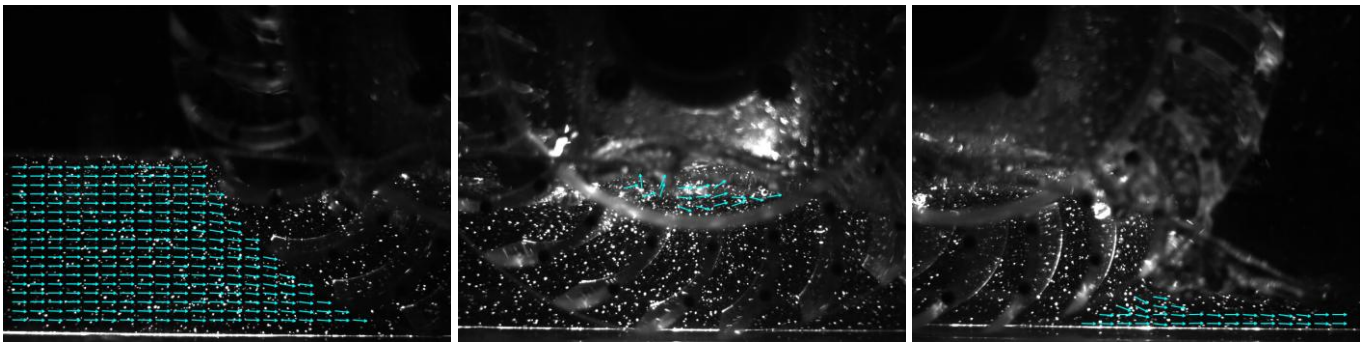

(a) Experiment

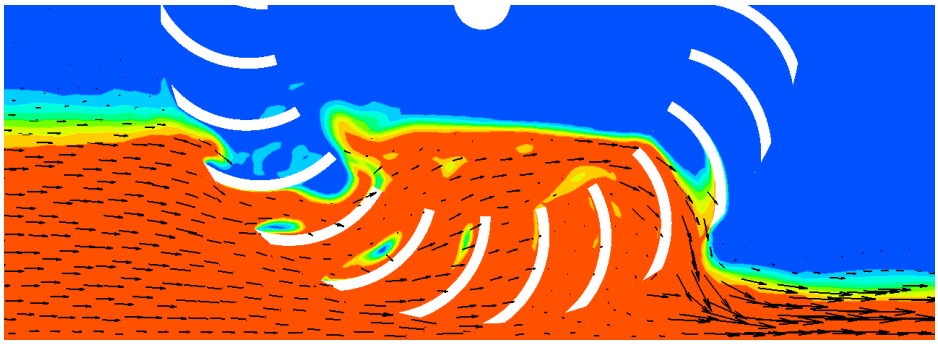

(b) Calculation

Fig. 8 Absolute velocity vectors at the circumference of the undershot runner (n = 22 min^{-1})

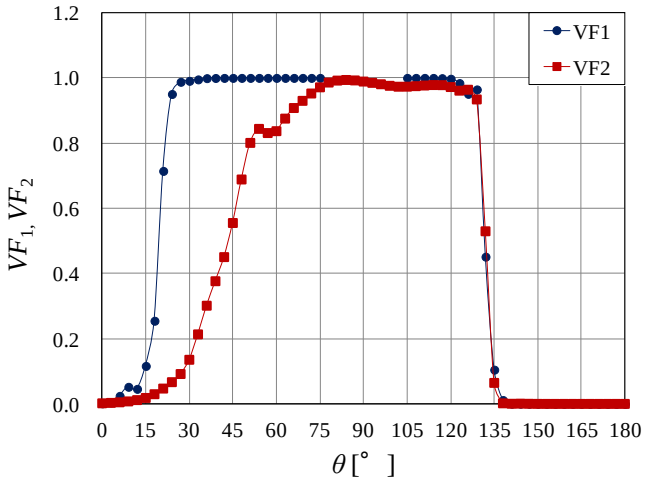

Fig. 9 Volume fraction of water at the runner's outer (VF_1) and inner (VF_2) circumferences (n = 22 min^{-1}, Cal.)

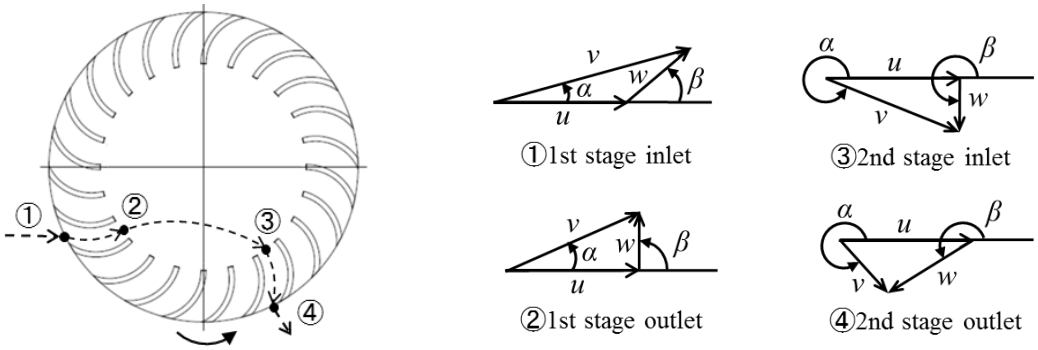

Fig. 10 Velocity triangles at the runner inlet (points 1 and 2) and outlet (points 3 and 4)

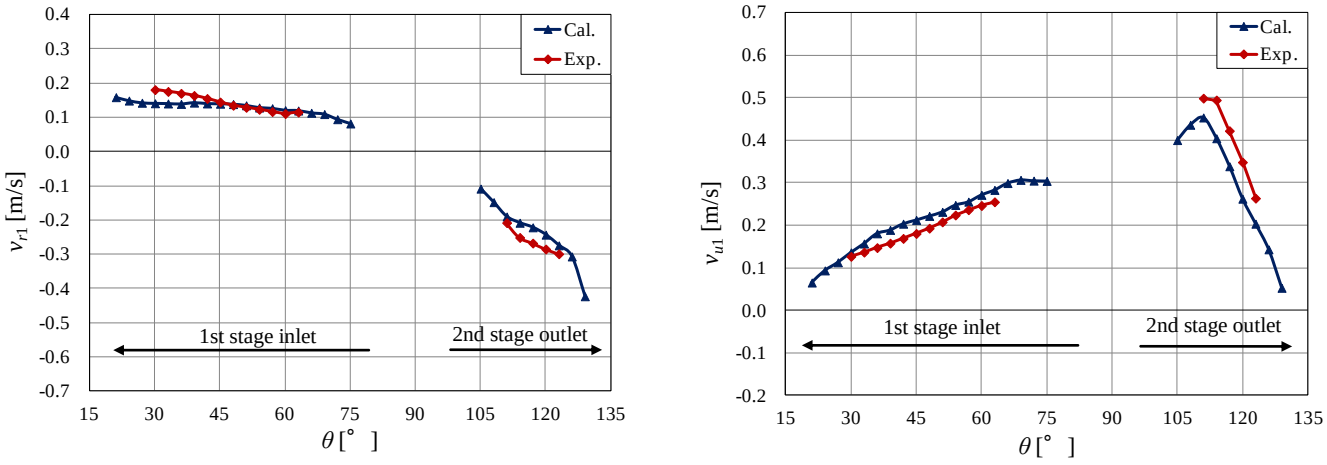

(a) Radial component (b) Circumferential component

Fig. 11 Absolute velocities at the outer circumference as determined by experiment and numerical analysis (n = 22 min^{-1})

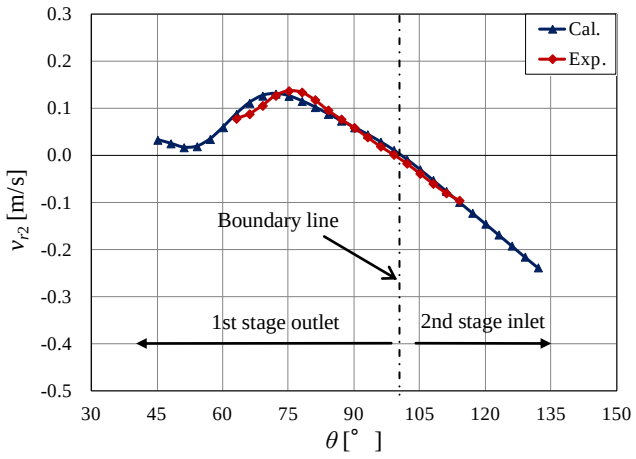

(a) Radial component

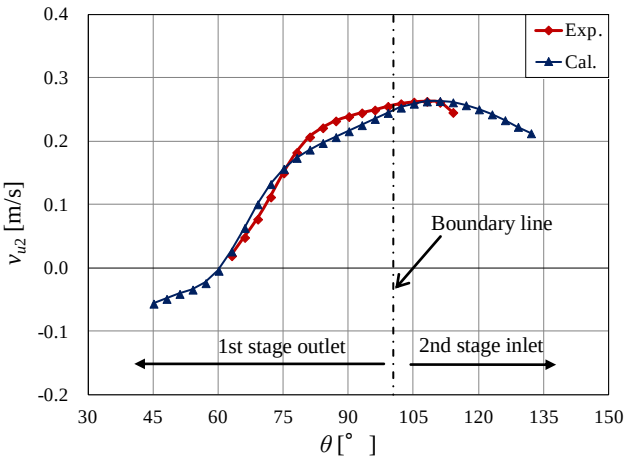

(b) Circumferential component

Fig. 12 Absolute velocities at the inner circumference as determined by experiment and numerical analysis (n = 22 min^{-1})

5. Conclusion

The performance of an undershot cross-flow turbine and the flow fields involving a free surface were investigated by experiment and numerical analysis. As a result, the experimental and calculated results of the performance and flow fields of this water turbine were found to satisfactorily agree. Moreover, the flow fields of this water turbine in the first stage inlet and outlet regions and the second stage inlet and outlet regions were clarified. Within the low θ region of the first stage outlet, the water is observed to be flowing backwards between the back blades. Furthermore, in the second stage outlet region, it is established that the flow has rapidly converted to the mainstream direction.

Nomenclature

B	Channel width [m]	v	Absolute velocity [m/s]
b	Runner width [m]	w	Relative velocity [m/s]
D	Runner diameter [m]	Z	Number of blades
g	Gravitational acceleration [m/s^2]	α	Absolute flow angle [°]
H	Effective head [m] (= $h_3 + v_3^2/2g - h_4 - v_4^2/2g$)	β	Relative flow angle [°]
h	Water depth [m]	β_b	Blade angle [°]
n	Rotational speed [min^{-1}]	γ	Clearance between runner and side walls [m]
P	Output power [W] (= $2\pi nT/60$)	δ	Clearance between runner and floor [m]
Q	Flow rate [m^3/s]	η	Turbine efficiency (= $P/\rho gQH$)
T	Torque [N・m]	θ	Circumferential angle [°]
u	Circumferential velocity [m/s]	ρ	Fluid density [kg/m^3]
VF	Volume fraction of water		

Subscripts

1	Inner circumference of runner	4	Downstream
2	Outer circumference of runner	r	Radial component
3	Upstream	u	Circumferential component

References

[1] C. Nicolet, A. Zobeiri, P. Maruzewski, F. Avellan, 2011, “Experimental Investigations on Upper Part Load Vortex Rope Pressure Fluctuations in Francis Turbine Draft Tube,” International Journal of Fluid Machinery and Systems, Vol. 4, No. 1, pp. 179-190.

[2] T. Vu, M. Koller, M. Gauthier, C. Deschênes, 2011, “Flow simulation and efficiency hill chart prediction for a Propeller turbine,” International Journal of Fluid Machinery and Systems, Vol. 4, No. 2, pp. 243-254.

[3] T. S. Reynolds, 1983, “Stronger Than A Hundred Men: A History of the Vertical Water Wheel,” The Johns Hopkins University Press.

[4] Y. Fujiwara, H. Kado and Y. Hosokawa, 1987, “History and Performance of Traditional Water wheel in Western Europe,” Transactions of the Japan Society of Mechanical Engineers, Vol. 90, No. 819, pp. 212-218. (in Japanese)
[5] A. Furukawa, S. Watanabe, D. Matsushita and K. Okuma, 2010, “Development of ducted Darrieus turbine for low head hydropower utilization,” Current Applied Physics, Vol. 10, pp. 128-132.
[6] Y. Choi, J. Lim, Y. Kim and Y. Lee, 2008, “Performance and Internal Flow Characteristics of a Cross-Flow Hydro Turbine by the Shapes of Nozzle and Runner Blade,” Journal of Fluid Science and Technology, Vol. 3, No. 3, pp. 398-409.
[7] J. D. Andrade, C. Curiel, F. Kenyery, O. Aguillón, A. Vásquez and M. Asuaje, 2011, “Numerical Investigation of the Internal Flow in a Banki Turbine,” International Journal of Rotating Machinery, pp. 1-12.
[8] J. Matsui, 2010, “Internal Flow and Performance of the Spiral Water Turbine,” Turbomachinery, Vol. 38, No. 6, pp. 358-364. (in Japanese)
[9] J. Matsui, 2012, “Internal Flow and Performance of the SpiralWater Turbine : 2nd Report : Model Experiment and CFD under Inclined Axis Operation,” Turbomachinery, Vol. 40, No. 2, pp. 91-96. (in Japanese)
[10] C. A. Mockmore and F. Merryfield, 1949, “The Banki Water Turbine,” Bulletin Series, 25.
[11] J. Fukutomi, 2000, “Characteristics and Internal Flow of Cross-Flow Tubine for Micro Hydro Power,” Turbomachinery, Vol. 28, No. 3, pp. 156-163. (in Japanese)
[12] Y. Nishi, T. Inagaki, R. Omiya, T. Tachikawa, M. Kotera and J. Fukutomi, 2011, “Study on a Cross-Flow Water Turbine Installed in an Open Channel,” Turbomachinery, Vol. 39, No. 8, pp. 467-474. (in Japanese)
[13] Y. Nishi, T. Inagaki, Y. Li, R. Omiya and J. Fukutomi, 2014, “Study on an Undershot Cross-Flow Water Turbine,” Journal of Thermal Science, Vol. 23, No. 3, pp. 239-245.
[14] ANSYS, Inc., 2010, “ANSYS CFX-Solver Theoretical guide,” pp. 137-139. (in Japanese)
[15] ANSYS, Inc., 2010, “ANSYS CFX-Solver Modeling guide,” pp. 144-145. (in Japanese)